Optical ray-tracing simulation method for the investigation of radiance non-uniformity of an integrating sphere

Martin Vacula[a,b], Pavel Horvath[a,*], Ladislav Chytka[b], Kai Daumiller[c], Ralph Engel[c,d], Miroslav Hrabovsky[a], Dusan Mandat[a,b], Hermann-Josef Mathes[c], Stanislav Michal[a,b], Miroslav Palatka[a,b], Miroslav Pech[a,b], Christoph M. Schäfer[c], Petr Schovanek[a,b]

[a] *Palacký University Olomouc, Faculty of Science, Joint Laboratory of Optics of Palacký University and Institute of Physics of the Czech Academy of Sciences, 17. listopadu 1192/12, 779 00 Olomouc, Czech Republic*
[b] *Institute of Physics of the Czech Academy of Sciences, Joint Laboratory of Optics of Palacký University and Institute of Physics of the Czech Academy of Sciences, 17. listopadu 1154/50a, 779 00 Olomouc, Czech Republic*
[c] *Karlsruhe Institute of Technology (KIT), Institute for Astroparticle Physics, Hermann-von-Helmholtz-Platz 1, 76344 Eggenstein-Leopoldshafen, Germany*
[d] *Karlsruhe Institute of Technology (KIT), Institute of Experimental Particle Physics, Hermann-von-Helmholtz-Platz 1, 76344 Eggenstein-Leopoldshafen, Germany*

Abstract

The paper deals with possibilities and limits of optical simulations of extended uniform light sources. Optical simulations of ideal and real light sources are performed using optical ray-tracing software which is capable to simulate non-imaging systems such as Lambertian disc and integrating spheres. The simulation methodology is validated by comparing the developed simulation model with a real experiment previously performed in optical laboratory. The comparison is made on the radiance uniformity measurement and simulation results of a general purpose integrating sphere rather than on less convenient and more frequent irradiance uniformity measurements. The aim is to develop a reliable simulation method for the investigation of radiance non-uniformity of any real extended uniform light source.

Keywords: Extended uniform light source, Lambertian disc, Integrating sphere, Virtual prototyping, Optical ray-tracing simulation, Radiance uniformity

1. Introduction

The development of any device generally begins with the preliminary design, followed by the production of the first physical prototype. The physical prototype is the key step in the development of a novel or innovative device. The device is designed to achieve the desired parameters which are then validated by the prototype under real conditions. After a comparison of desired and real parameters is made, necessary modifications are made in the construction of the device and another iteration is performed until the desired device parameters are met. This ongoing process leads to the formation of the final device. Unfortunately, such an approach is very expensive and time consuming. Therefore, a different approach of the device development is becoming more popular. This method is known as virtual prototyping [1–3] and it is on a rapid increase in many applications including optical research. Due to the existence of optical simulating software of sufficient accuracy, virtual prototyping limits the need for physical prototypes to the minimum. Moreover, modifications and alternative variants of the device are designed much more easily. All of this results in lower costs and faster creation of the final virtual prototype in contrary to a physical prototype. Among other things, virtual prototyping is used to design and analyze both imaging and non-imaging optical

*Corresponding author
Email address: pavel.horvath@upol.cz (Pavel Horváth)

systems and devices. There are quite a lot of software packages intended for optical simulations. They can be divided into two groups depending on the purpose of the simulation.

First, sequential optical ray-tracing is used to design imaging systems [3–5]. This type of ray-tracing is based exclusively on the laws of refraction and reflection, while the rays are passing through a sequence of optical surfaces and optical media interfaces. Most known commercial software using this type of ray-tracing are CODE V (Synopsys, Inc.) [6], OpticStudio (Zemax LLC) [7], OSLO (Lambda Research Corporation) [8], etc. However, sequential ray-tracing does not allow to simulate, for example, the diffuse transparent and reflective optical surfaces and the repetitive passage or reflection on the same optical surfaces and the like. Second, the non-sequential optical ray-tracing, used mainly for non-imaging systems, is not limited by the conditions of sequential ray-tracing [3–5]. Optical elements and sources are modeled as 3D objects instead of a sequence of optical surfaces. It can be used to simulate non-imaging systems such as various lighting systems, including automotive headlights. Examples of software utilizing non-imaging ray-tracing are TracePro (Lambda Research Corporation) [9], ASAP (Breault Research Organization, Inc.) [10], LightTools and LucidShape (Synopsys, Inc.) [11, 12].

At our laboratory, we have a long-term experience with the usage of OpticStudio software, which is mainly focused on the sequential ray-tracing for imaging systems simulation. However, a non-sequential module is included in the software as well. It allows to simulate less complicated non-imaging optical systems. The OpticStudio software can be applicable in terms of virtual prototyping of extended uniform light sources (EULSs) after successful verification on simpler examples of Lambertian disc (LD) and integrating spheres (ISs). The integrating sphere is a non-standard optical element in the shape of a spherical cavity with a diffuse reflective surface. It is obvious that it can be simulated only using the non-sequential optical ray-tracing.

There is a large amount of literature concerning ISs. It focuses on a wide range of theoretical descriptions relating to the principles of their function, various analyses, and specific applications. The practical use of ISs can be divided into three basic fields. Firstly, the oldest application is radiometric or photometric measurement of the optical properties of light sources [13, 14]. Secondly, the determination of optical properties of various materials, such as reflectance or transmittance [13, 15]. Third, the least common application is the use of ISs as an EULS to calibrate detectors (matrix CCD or CMOS cameras and arrays of PMTs or SiPMs sensors) [16, 17]. Over the years, fundamental "rules of thumb" have been established for the construction and selection of applications based on the long-term experience in designing ISs [15]. These rules are sufficient to determine the usability of ISs in the intended applications. The literature on ISs deals mainly with various analytical studies. However, less attention is paid to numerical optical simulations (virtual prototyping) of ISs. Moreover, optical simulations of ISs as EULSs are complicated by the method used in non-sequential ray-tracing. This method is called Monte Carlo ray-tracing and is based on randomly generated directions of optical rays, which results in statistical noise in optical simulations [4, 18]. Despite the statistical noise being negligible when the total value of the light flux is simulated at the output of an IS, it causes undesirable spatial high-frequency modulation in case of simulating its radiance or irradiance uniformity. The statistical noise that arises in the Monte Carlo ray-tracing is only present in the simulation and has nothing to do with the real radiance or irradiance uniformity at the output of the IS. Thus, the statistical noise needs to be minimized by selecting appropriate input parameters of non-sequential ray-tracing.

The first part of the paper is devoted to the verification of the applicability of the selected optical ray-tracing software to examples of simulations of ideal EULSs. Specifically, the LD of well-known theoretical properties [19, 20] followed by the example of an ideal IS [15, 21]. According to theory, their radiometric properties should be similar (almost identical). In addition, the level of statistical noise in the optical simulations for both cases should be acceptable (not exceeding the value of the real radiance or irradiance non-uniformity). Next, a more complicated model of a selected representative of a real general purpose IS by Labsphere (3P-GPS-053-SL) is simulated. This developed model and the simulation methodology are analyzed and commented in the second part of the paper. Finally, the simulation results of the model are compared with the results of measurement [22] of radiance uniformity of a general purpose IS. These measurements were performed using a designed experimental setup in our optical laboratory in 2020. The primary goal of the presented paper is to show the agreement between newly simulated and previously

measured results. This agreement will be a proof of the possible virtual prototyping using the developed simulation method for the investigation of sources of local non-uniformity based on the radiance of general purpose IS (as well as any real EULS).

2. Models of ideal extended uniform light sources

An ideal EULS is characterized by a well defined spatial radiation profile allowing for example a calibration of planar matrix detectors. The irradiance is constant at all points in the detector plane if it is located in close proximity to the ideal EULS and if its size is smaller compared to the EULS. Such a setup is commonly known as a near field. Unfortunately, the irradiance in the detector plane varies depending on the distance from the ideal EULS. It can be determined using the theory of the radiative transfer between two surfaces [23]. However, complex integral equations must be solved. An exact analytical solution of these equations can be found only in rare cases considering a very simple geometric arrangement of two planar surfaces (a source and a detector). An excellent example of the existence of an exact analytical solution is the case of two circular parallel surfaces, which is used for our analyses.

Consider a circular EULS with a radiance $L(x, y, \phi, \psi)$ and a circular detector of any radius and at any distance from the source according to the Fig 1. The irradiance $E(X, Y, \phi, \psi)$ at any point in the detector can be determined using

$$E(X, Y, \phi, \psi) = \int_{A_S} L(x, y, \phi, \psi) \frac{\cos\phi \cos\theta}{z^2} \, dA_S, \tag{1}$$

where the quantities ϕ and θ represent angles between the optical axis and the normals to the surfaces of EULS and detector at the intersection points (elements of areas da_s and da_d), respectively. The area of the EULS is A_S. The distance between two points is z. Angle ψ represents the rotation around the EULS normal [23].

In general case, the irradiance at an arbitrary pixel of a planar detector is given by the Eq. (1). However, it can be simplified in the case of the ideal Lambertian radiance assuming $L = const.$ for every location and direction. The integral equation Eq. (1) then follows the relation

$$E(X, Y, \phi, \psi) = L \int_{A_S} \frac{\cos\phi \cos\theta}{z^2} \, dA_S. \tag{2}$$

Furthermore, a solution of Eq. (2) can be found in the form of exact analytical formulas. This approach is applicable for ideal Lambertian sources (LD in Sec. 2.1 and ideal IS in Sec. 2.2).

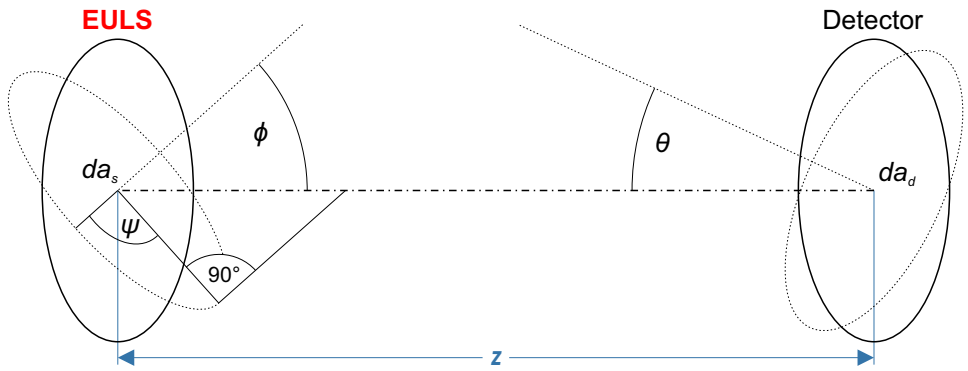

Figure 1: A layout of radiative transfer between two circular surfaces, an extended uniform light source (EULS) and a detector. The elements of the area surfaces da_s and da_d are linked by the optical axis. The distance between arbitrary elements of area surfaces is z. The angles between optical axis and normals to the surfaces of EULS and detector are ϕ and θ, respectively. The rotation around the normal of the EULS is represented by the angle ψ [23].

Derived from the properties of the circular EULS follows that from a certain distance, the spatial irradiance properties between a source and a detector are not changing anymore. It can be expressed by a simple mathematical formula known as the cosine-fourth-power law, which describes the decrease of the irradiance intensity from the center of the detector to its edge. The accuracy of this approximation to the exact analytical formula given by Eq. (1) for irradiance at the detector increases with the increasing distance between source and detector. The inaccuracy is converging to 1 % in the case where the distance of the detector to the source is a quintuple of the diameter of the source. This is one of the optical rules of thumb, called the "five times rule", which is widely respected during the assembly of laboratory setups for irradiance measurements, including the standards EMVA 1288 [24]. The five times rule distance is the limit for starting point of the far field measurements.

As mentioned in Sec. 1, the aim of the paper is to develop a simulation method designed for radiance non-uniformity investigation by cross-checking the results obtained by the simulation with the data from laboratory measurement [22]. For this purpose, a model of general purpose IS is developed to compare the radiance uniformity of the exit port of this IS. However, it is desirable to first verify the capabilities of the OpticStudio software for such an analysis. Since the high resolution radiance uniformity of the IS is to be studied, it has to be clear whether the statistics and precision of the selected optical ray-tracing software are sufficient for this task. Special attention needs to be paid to the correct optimization of the input parameters used in the optical simulations. It is advisable to perform simulations of undemanding models of EULSs prior to the simulation of rather complex real IS. Therefore, two theory-based models of EULS are developed prior to the analysis of the general purpose IS, they are represented by LD and ideal IS.

The verification of the applicability of the selected optical ray-tracing software simulations for virtual prototyping of ISs is based on the comparison of the results acquired from two theory-based models. First, results of the exact analytical models are obtained using mathematical equations. Next, results of the non-sequential ray-tracing models are acquired from optical simulation. Both models consider a surface detectors irradiated by the LD or IS. Presented results are calculated for several distances between the light source and a detector covering both near field and far field measurements. Distances are chosen in accordance with the literature [20].

2.1. Model of Lambertian disc

The initial step of analysis is to use the exact analytical model and derive an appropriate expression for the irradiance at a detector originating from a LD. The LD is a circular plane with a radius R, a uniform radiance L, and with Lambertian radiation. Consider a planar irradiance detector parallel to the light source (LD) at a distance z. The irradiance at an arbitrary pixel of the detector at a distance r from the optical axis of the LD is given by

$$E_r = \left(\frac{\pi L}{2}\right)\left\{1 - \left[1 + \frac{4R^2z^2}{\left(z^2 + r^2 - R^2\right)^2}\right]^{-1/2}\right\}. \tag{3}$$

By letting $r = 0$, the irradiance at the axial point of the LD is obtained as

$$E_0 = \frac{\pi L R^2}{(R^2 + z^2)}. \tag{4}$$

It is clear that the irradiance is maximal at the axial point of the detector. The derivation of the Eqs. (3) and (4) is described in detail in [20].

The simplest theory-based model is the LD. To study the dependence of the normalized irradiance E_r/E_0 on the normalized ratio of distances r/z (ending at value 2 [20]), the exact analytical calculations are done using Eqs. (3) and (4). The radius R of the LD is set to 25 mm, the distance z is then calculated according to the selected ratios of z/R (1, 2, 5, 10, and 100) as 25 mm, 50 mm, 125 mm, 250 mm, and 2500 mm respectively. The next step is to compare the theoretical values with the optical ray-tracing simulation.

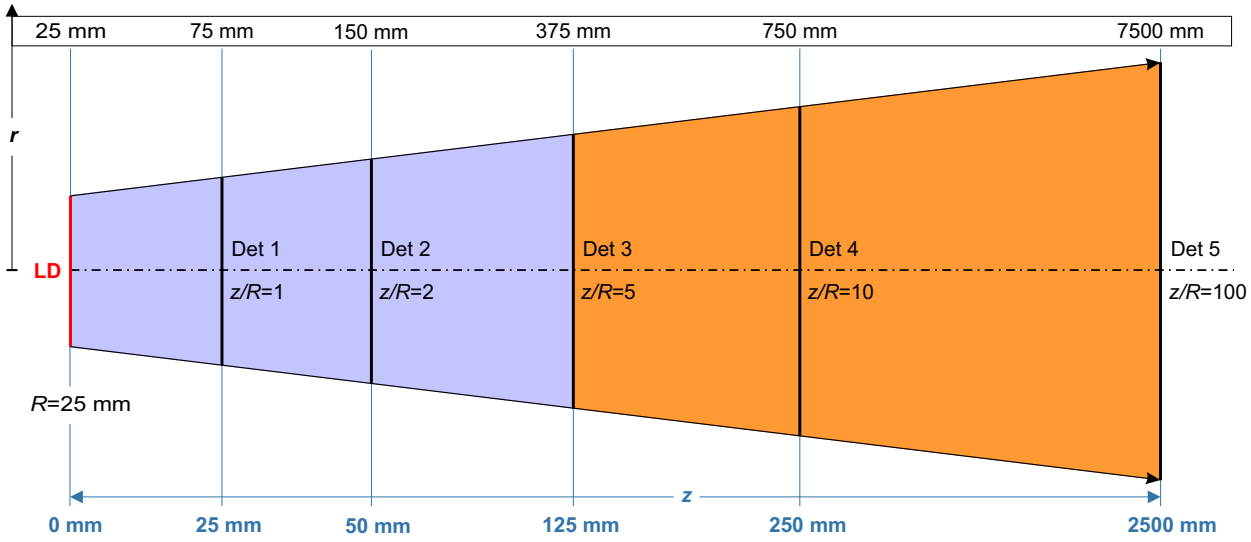

Figure 2: Layout of both the exact analytical model and the optical simulation using a logarithmic scale for better interpretation of the distances and radii. Circular Lambertian disc (LD) of the radius R and five detectors with radii r (listed in a bar at the top of the figure) located at distances z (listed below the axis) in a way that the angular field of view of the LD is the same for each detector. The ratios z/R distinguishing the near field (violet) and the far field (orange) are denoted for every detector.

In the optical simulation, the LD and corresponding detectors are modeled using the above-mentioned geometrical parameters. The model consists of a circular light source with Lambertian (cosine) emission profile of the radius R=25 mm and five rectangular detectors at selected distances. The schematic image of the theoretical models is shown in the Fig. 2. Since the optical ray-tracing analysis is affected by statistical fluctuations, a smoothing function is used to obtain more accurate results. For this purpose, the built-in Optics studio moving average is used [25].

The results of the normalized irradiance E_r/E_0 for both the exact analytical model and the optical simulation of Lambertian disc are shown in the same plot, see Fig. 3. Whereas the results of the exact analytical model are depicted as black curves, the results of the optical simulation are colored (dashed curves). Every individual curve of the normalized irradiance E_r/E_0 of the exact analytical model corresponds to the optical simulation, according to the ratio z/R.

By letting $z \gg R$, the Eq. (3) limits in the cosine-fourth-power law

$$E_e \approx E_0 \cos^4 \phi = E_0 \left(\frac{z}{\sqrt{r^2 + z^2}} \right)^4 , \tag{5}$$

where ϕ is the angle at which the arbitrary pixel of the detector is visible from the center of LD. Note that the higher the ratio z/R is, the better the curve corresponds to the cosine-fourth-power law, see Fig. 3 [20, 22, 26]. When the ratio z/R exceeds the five times rule, the simulated data start to correspond with the theoretical cosine-fourth-power law and with the ratio $z/R \approx 100$ and higher, they correspond nearly perfectly.

To express the agreement between models numerically, the normalized values of the Mean Absolute Error (MAE) of the exact analytical model (prediction) and optical simulation (value acquired from the ray-tracing simulation) are evaluated for every ratio z/R. The MAE follows the relation

$$\mathrm{MAE} = \frac{1}{n} \sum_{i=1}^{n} |e_i| = \frac{1}{n} \sum_{i=1}^{n} |y_i - x_i| , \tag{6}$$

where the terms $|e_i|$ are the absolute errors of the optical simulation represented by the difference between the terms of the exact analytical model y_i and the optical simulation x_i [27]. Since the MAE from Eq. (6)

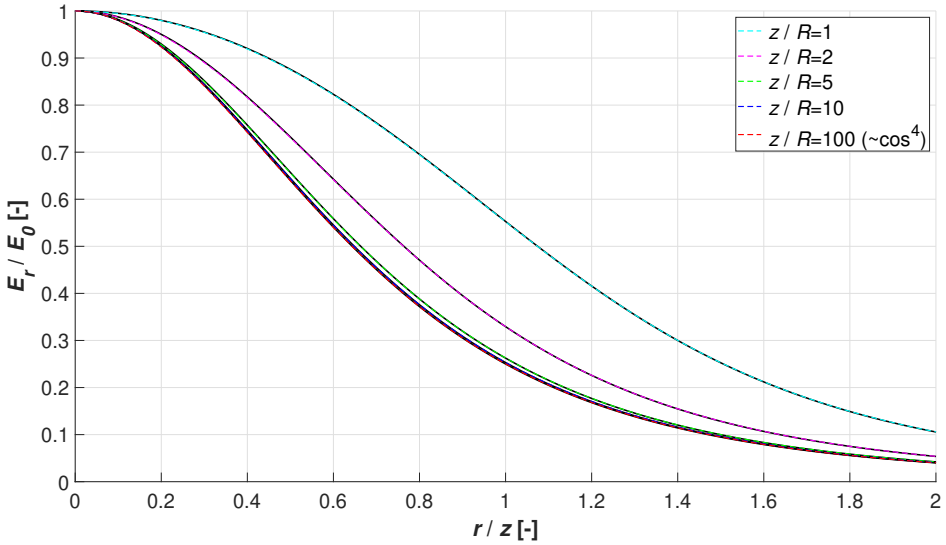

Figure 3: The dependence of the normalized irradiance E_r/E_0 on the normalized ratio of distances r/z. Exact analytical curves are depicted in black while the results of the optical simulation of Lambertian disc (LD) are shown by the color dashed curves. The plot shows the comparison of analytically calculated results with the simulation model of LD for five selected ratios of z/R.

is a scale-dependent parameter, the relative values of the difference between the exact analytical model and the optical simulation are obtained by a simple normalization

$$\text{MAE } [\%] = \frac{1}{n}\sum_{i=1}^{n} |y_i - x_i| \, \frac{100}{y_i}. \tag{7}$$

The normalized values of MAE are listed in Table 1 as MAE^{LD} (Lambertian disc).

Ratio	$z/R = 1$	$z/R = 2$	$z/R = 5$	$z/R = 10$	$z/R = 100$
$\mathbf{MAE}^{LD}$ **[%]**	0.224	0.278	0.336	0.334	0.331

Table 1: Normalized MAE^{LD} (results of Lambertian disc) values calculated according to the Eq. (7). These error values of the optical simulation demonstrate the quantitative difference between results of normalized irradiance E_r/E_0 determined by the exact analytical model and the optical simulation from Fig. 3. The results are presented for five selected ratios of distances z/R.

2.2. Model of the ideal integrating sphere

A more complex theory-based model presented prior to the model of general purpose IS is the ideal IS. Again, the model is based on the handy rules of thumb obtained by the experience while working with ISs. However, the developed model presented in this paper intentionally exceeds these rules (specifically ratio of diameters of the exit port and inner cavity) for better comparison with the model of the ideal LD. In theory, there should be no difference, because the exit port of the IS is actually a virtual LD with the same diameter. In reality, some differences are, of course, expected because of the multiple reflections inside the sphere, where the rays reflect and scatter on the inner surface of the sphere until they leave the cavity through the exit port of the IS. The most significant difference between LD and an ideal IS regarding the simulation is that the inner diameter of an ideal IS is ten times larger then the diameter of its exit port (corresponds to a virtual LD). Thus, the area of the exit port is four hundred times smaller than the area

of the inner cavity. Simply, four hundred times more rays are needed to ensure the same amount of rays on the exit port of the IS to maintain the same conditions. This will, of course, have a significant impact on computational times.

Nevertheless, the exact analytical model of the ideal IS is developed similar to the case of LD, where the exit port of the IS has a radius R and a radiance L with planar irradiance detectors at a distance z parallel to the source (exit port of the IS). Again, the objective is to study the dependence of normalized irradiance E_r/E_0 on the normalized distance ratio r/z (ending at value 2 [20]) according to the Eqs. (3) and (4) described in the Sec. 2.1. To preserve the same parameters, the radius of the exit port is set to 25 mm and the distance z remains the same according to the selected ratios of z/R (1, 2, 5, 10, and 100) as 25 mm, 50 mm, 125 mm, 250 mm, and 2500 mm respectively. The values calculated from the exact analytical model for these parameters are plotted in Fig. 4 as black curves. The comparison with the exact analytical model is done by the optical ray-tracing simulation. The results of the optical simulation of ideal integrating sphere are represented by colored dashed curves in Fig. 4.

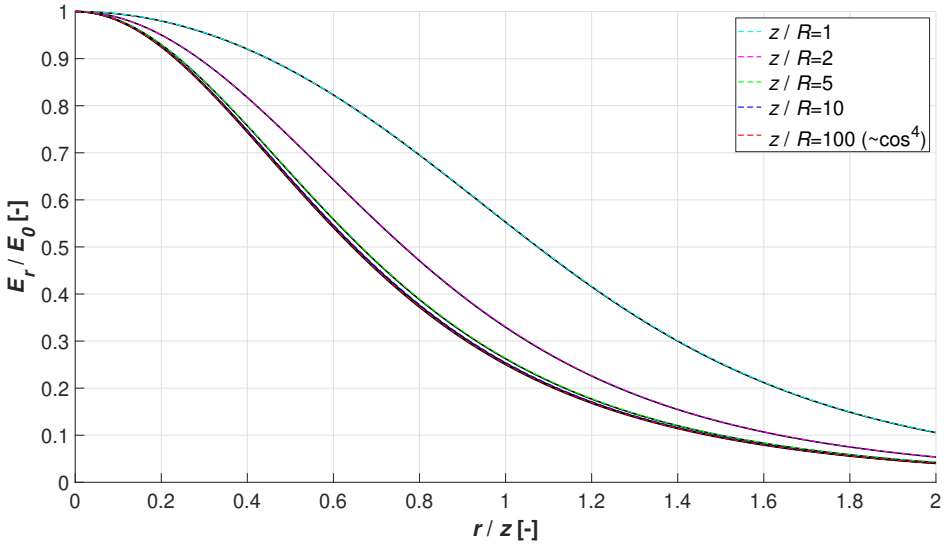

Figure 4: The dependence of normalized irradiance E_r/E_0 on the normalized ratio of distances r/z. Exact analytical curves are depicted in black while the results of the optical simulation of ideal integrating sphere (IS) are shown as color dashed curves. The plot shows the comparison of analytically calculated results to the simulation model of the ideal IS for five selected ratios of z/R.

The optical simulation consists of an IS, a circular light source of negligible size (point source) and detectors. The IS in the simulation is considered ideal by selecting specific p arameters. T he r eflectance of the inner cavity is set to 100 % (no loss in energy after reflection), t he s cattering i s s et t o 100 % (meaning that every ray incident on the surface scatters), and the number of rays created from every hit on the surface is 1 (no ray splitting is applied and therefore the rays only change direction). The radius of the exit port of IS corresponds to the radius of the LD and is equal to 25 mm. Since the recommended ratio of diameters of the exit port and inner cavity (to achieve the radiance uniformity of 99 % or better) is 4 or higher, the radius of the IS is set to 250 mm and thus the ratio is 10 [28]. The actual circular light source with Lambertian (cosine) emission profile o f t he r adius 0.1 m m i s s situated i nside t he I S n ear t he e xit p ort a nd i t i s facing to the back surface of the IS. Together, they form the virtual source (exit port of the IS) with a radius of 25 mm. Finally, five r ectangular d etectors a re p laced a t a bove m entioned d istances t o r eproduce t he same plot as in Fig. 3. Again, it is evident that the curve corresponds with the cosine-fourth-power law better with increasing ratio z/R.

The normalized values of MAE are evaluated for every ratio z/R and listed in Table 2 as MAE^{IS} (integrating sphere).

Ratio	$z/R = 1$	$z/R = 2$	$z/R = 5$	$z/R = 10$	$z/R = 100$
MAE^{IS} [%]	0.322	0.394	0.475	0.472	0.496

Table 2: Normalized MAE^{IS} (results of integrating sphere) values calculated according to the Eq. (7). The error values of optical simulation show the quantitative difference between results of normalized irradiance E_r/E_0 determined by the exact analytical model and the optical simulation from Fig. 4. The results are presented for five selected ratio of distances z/R.

3. Model of a general purpose integrating sphere

After proving that the selected optical ray-tracing software meets the requirements for the precision of the desired simulations of the EULSs, the final optical simulation can be performed. However, the design of particular ISs differs according to the way they are used [13, 21]. The most crucial factor that alters the design of ISs is the geometry of the inner cavity determined by the arrangement of ports, detectors and baffles. These components have a significant impact on the radiance uniformity of the inner surface of ISs. Thus, there is no universal, commonly used model of a real IS. For the presented study regarding optical simulations, a real general purpose IS by Labsphere (3P-GPS-053-SL) is chosen, because its parameters were already measured in detail. The idea behind this simulation is to reproduce the results of the laboratory measurement [22]. The goal is to determine to what extent the results of the optical simulations can correspond to the results measured in our laboratory. Validating the accuracy of the optical simulation model on a specific example of a general purpose IS will therefore allow for future analyses or applications such as virtual prototyping of ISs based on the simulation method simulating the radiance uniformity. This method excels in locating the sources of non-uniformity.

3.1. Development of the optical simulation model

The geometry of the specific real general purpose IS by Labsphere (3P-GPS-053-SL) can be found in the manufacturer's datasheet [29]. Other important parameters can be obtained by measurement. Crucial are the precise position and dimensions of a baffle inside the IS cavity. These two parameters have the largest influence on the level of the radiance uniformity inside the IS and thus on the radiance uniformity at the exit port of the IS. Therefore, the baffle could be referred to as the "geometric error" of the inner cavity of IS [14] and has to be modeled exactly according to the datasheet. The other component that brings the radiance non-uniformity to the inner cavity and thus at the exit port as well is the input light source. In optical simulations, the narrow conical beam should result in a brighter "hot spot" on the surface of the inner cavity of the real IS. However, the theory and the model of an ideal IS do not assume the existence of hot spots. Since the exit port of a real IS is only a virtual source, the actual input light source is a key part of the optical simulation. For the optical simulation model of a general purpose IS, a Fiber-Coupled LED (FC-LED) with a core diameter of the optical fiber of $d = 400\,\mu\text{m}$ and with a numerical aperture of $\text{NA} = 0.22$ is intentionally chosen as an input light source to reproduce the previously performed measurement [22]. The output of this FC-LED is a light beam with the divergence of about 25° and a wavelength of 365 nm.

Having the input light source modeled and knowing the exact geometry of the desired IS, the simulation model can be developed accurately, however with one limitation. The infill of the inner cavity of the selected general purpose IS is made of Spectralon. This is a diffuse reflective bulk (volume) PTFE material [30, 31]. Thus, the diffuse reflection and scattering of the incident rays are affected also by the layers under the surface. To achieve a high diffuse reflectance on the Spectralon (above 99 %), it needs to be at least 6 mm thick. However, it is practically impossible to simulate such a layer of bulk material in selected optical ray-tracing software. Thus, it is replaced by simple diffuse reflective surface with the reflectance of 99 % (coating) and the ideal Lambertian scattering profile referred to the theoretical model of the Lambertian surface [23, 26] for a wavelength of 365 nm. This approach does not significantly affect the accuracy of the optical simulation. The simplified layout of the simulated general purpose IS is depicted in Fig. 5 for two representative points of view of the 3D layout to show the conical profile of the FC-LED and uniformly distributed rays that have been scattered after the first strike. All the components regarding the optical

simulation model are clearly seen as well. Figures 5a), and 5b) represent the front view and Figs. 5c) and 5d) represent the side view. For the simulations, the fibre source is located at the top of the IS.

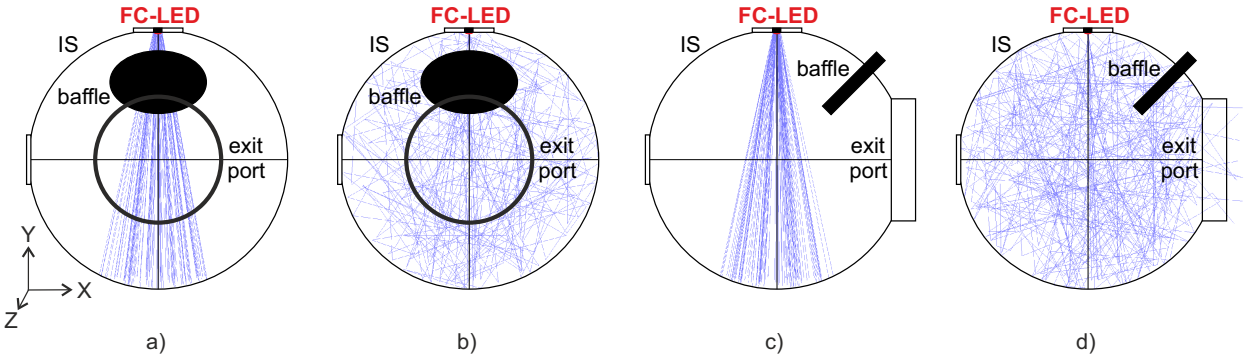

Figure 5: The simplified 3D layout of the simulated general purpose IS with a baffle, exit port and FC-LED light source. a) the front view with 100 rays displayed until the first strike, b) the front view with 10 rays and Lambertian scattering, c) the side view with 100 rays displayed until the first strike, d) the side view with 10 rays and Lambertian scattering.

3.2. Optical simulation

Evaluation of the results for both theory-based models (LD and ideal IS) is straightforward. In both cases, all exact analytical models and optical simulations consist of ideal circular sources with a Lambertian emission profile. Due to the rotational symmetry of the sources, the same results are obtained in all directions from the center to the edge of the detector in a given plane parallel to the source. Therefore, it is sufficient to analyze the irradiance at planar detectors at specific distances in the form of a single curve. The curve describes the decrease of the irradiance from the center of the detector to its edge for an arbitrary angle in the detector plane.

On the other hand, in the case of the optical simulation of a real IS, the evaluation method has to be modified due to its a symmetry. In this particular case, the baffle is situated between two ports and creates an asymmetry of the radiance at the exit port of the IS. Thus, it is expected that the irradiance at a planar detector at arbitrary distance will be asymmetrical as well. Therefore, evaluation of the results in one axis is no longer a valid option, as it is for the ideal symmetrical cases.

The irradiance $E(X, Y, \phi, \psi)$ of an arbitrary pixel of a planar detector parallel to the EULS is given by the sum of all radiating points of such a source. It can be calculated by integrating the radiance of the source over its surface A_S. In general, the radiance L of an EULS is a function of location and direction. The location on the surface of the source is given by two spatial variables (x, y) while the direction of the radiance emitted is given by two angular variables (ϕ, ψ). All together, they form the function of the radiance $L(x, y, \phi, \psi)$. For some cases of simpler geometries, the value of the irradiance at a detector plane can be calculated by solving numerically the integral equation (case of LD and ideal IS). However, the geometry of a real IS is not simple and the radiance $L(x, y, \phi, \psi)$ is not constant over the location and direction. The integral equation of the irradiance at the detector plane practically does not have an exact analytical solution that could be compared with the results of the optical simulation of a real IS. Therefore, a different comparison approach has to be chosen to validate the accuracy of the optical simulation model in contrast to the optical simulations of the ideal Lambertian sources used in Sec. 2.

The results of the optical simulation of general purpose IS can be compared to the results of the laboratory measurement [22]. However, the interpretation of the irradiance results is rather problematic and the use of such results is limited, because the irradiance at a detector plane is generally a function of the radiance $L(x, y, \phi, \psi)$. Thus, it does not provide the information of the position of the source of non-uniformity. Due to this fact, it is much more convenient and informative to work directly with the radiance. The radiance measurement of the EULS as a function of location and direction is in general a difficult and complex process, but it can be simplified under certain assumptions. The principle of the simplification is following.

The Eq. (1) for the irradiance $E(X, Y, \phi, \psi)$ can be rewritten as

$$E(X, Y, \phi, \psi) = \int_{\Omega} L(x, y, \phi, \psi) \cos\phi \; d\omega = \int_{\phi} \int L(x, y, \phi, \psi) \cos\phi \sin\phi \; d\phi \; d\psi. \tag{8}$$

So, the integration of the radiance $L(x, y, \phi, \psi)$ over the area of an EULS A_S in the Eq. (1) is changed to the integration over the solid angle Ω in the Eq. (8). Furthermore, the element of the solid angle $d\omega$ can be divided into two angular components $d\phi$ and $d\psi$. The solid angle Ω is defined by the size of an EULS. In specific cases it is thus sufficient to integrate only over a certain solid angle instead of integrating over the entire hemisphere. However, in the most general cases, the irradiance at an arbitrary pixel of a planar detector is given by the integration of the radiance over the entire hemisphere [23, 32].

Integration can be considered as the sum of infinitesimal elements. An EULS is thus considered as the sum of infinitesimal point sources. To be more precise, the sum of infinitesimal patch areas dA_S. The infinitesimal element of the solid angle $d\omega = \sin\phi \; d\phi \; d\psi$ is angle subtended by a patch area dA_S and by the distance from the detector z. Consider an EULS divided into a finite number of patch areas N of a non-infinitesimal size. With such an assumption, the integral in the Eq. (8) can be replaced by a summation. Therefore, an EULS is considered as the sum of a large number of small light sources

$$E(X, Y, \phi, \psi) = \sum_{i=1}^{N} L(x, y, \phi, \psi)_i \cos\phi_i. \tag{9}$$

It is obvious that the computational accuracy using Eq. (9) will decrease when the number of patch areas N decreases and their size increases at the same time. The radiance of each i-th patch area $L(x, y, \phi, \psi)_i$ is the average radiance of all infinitesimal point sources inside this patch a rea. To experimentally determine the radiance, a specific instrument called radiance detector (RD) is used [22]. The field of view (FoV) aperture of this RD directly defines the size of patch area $d\ A_S$ related on its distance from the EULS. On the other hand, the irradiance $E(X, Y, \phi, \psi)$ at the detector plane is the sum all patch areas of the examined EULS.

Nevertheless, the function of the radiance $L(x, y, \phi, \psi)$ can be in principle simplified by dividing it into the spatial $L(x, y)$ and the angular $L(\phi, \psi)$ radiance components during the measurement process with RD. Moreover, some of the spatial or angular components can be fixed in a way that they have zero or a constant value for a partial measurement procedure with RD. For the spatial radiance measurement, angular components are fixed as constants c_ϕ, $c_\psi$while spatial components x, y are variables, hence $L(x, y, c_\phi, c_\psi)$. For example, the spatial radiance of the EULS for N patch areas can be measured in perpendicular direction to the source area when the angular coordinates ϕ and ψ are equaled zero, simply $L(x, y, 0, 0)$. On contrary to the spatial radiance measurement, angular radiance is measured by fixing the spatial coordinates x and y. The simplest way is to also fix one of the angular components and measure the angular radiance in only one direction, e.g., $L(c_x, c_y, \phi, c_\psi)$, where c_x, c_y, c_ψ are constants. Angular radiance can be, as well as the spatial radiance, measured for N patch areas. However, it would be incredibly time consuming. Therefore, only a few representative patch areas with appropriately chosen spatial coordinates x and y are measured. Usually one in the center, and several between the center and the edges of the EULS, depending mainly on its geometry.

Based on the above mentioned principle, the influence of the geometrical arrangement of the inner cavity of IS on the radiance and the irradiance uniformity can be examined by the laboratory measurement. The radiance based measurement is a great way to study the dependence of changes in the geometrical arrangement on the radiance or the irradiance uniformity of EULSs. Moreover, it is possible to use this method in the virtual prototyping and optical simulations by simulating the effect of RD. In this way, the correspondence of the simulated results with reality (measurements) can be evaluated. Of course, the uncertainty in accuracy due to imperfections of the simulation model has to be taken into account.

In optical ray-tracing softwares, besides the irradiance distribution at a planar detector, both the spatial radiance $L(x, y)$ and the angular radiance $L(\phi, \psi)$ can be simulated as well. The detectors are the key parts of the optical simulation model in terms of uniformity evaluation. All detector parameters of the simulation are thoroughly chosen according to the previously performed laboratory measurement [22]. Thus, to evaluate

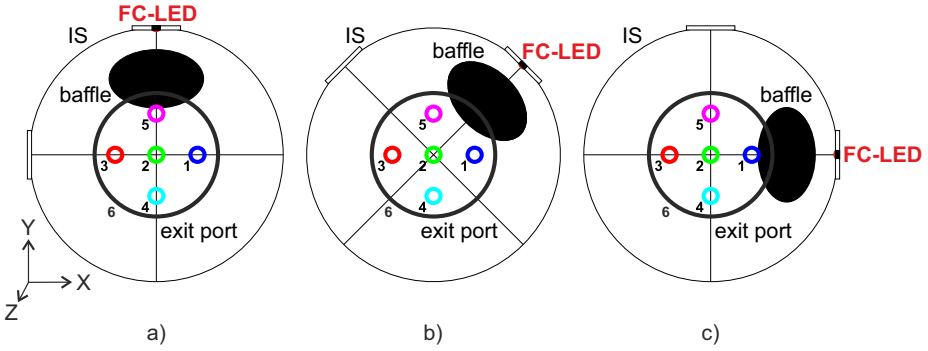

Figure 6: Front view of the 3D simplified layout of the simulated general purpose IS with detectors. The angular detectors are set inside the color circles (spots) 1–5 in the exit port and represent the selected positions of angular measurement [22]. The spatial detector is set inside the black circle 6 and covers the whole exit port aperture. The rotation positions are a) vertical, b) diagonal, and c) horizontal depending on the position of the light source (FC-LED) and the baffle.

both the spatial and angular uniformity results of the simulation in one run, a total of six dedicated detectors are used (see Fig. 6). Five representative spots of angular radiance uniformity measurement are simulated by corresponding rectangular (square) detectors, with circular annular surfaces in front of them, sensitive to the direction of incident rays with the maximal cone of 23°. The last and largest detector, covering the whole exit port aperture, is used to simulate the spatial radiance uniformity measurement. This detector is thus restricted with a near normal filter. The filter enables only the detection of rays with incident direction cosine greater than the value 0.9998. This condition corresponds to the maximum Field of View (FOV) of the Radiance Detector (RD) used in the laboratory measurement (2.29°).

3.3. Results of the simulation and the comparison with the laboratory measurement

To validate the developed model, a comparison with the laboratory measurement is done. In Fig. 7a) and 7b), there are the results of the spatial radiance uniformity measurement [22]. In Fig. 7c) and 7d), there are corresponding results acquired by the simulation. The spatial radiance measurement and simulation followed the prescription of radiance function $L = (x, y, 0, 0)$. Thus, only the spatial coordinates of the radiance function are variables. For all plots in Fig. 7, a normalization procedure is applied. Color-maps in the Fig. 7a) and c) are presented in fine range of 95 % - 100 % and the highest (maximum) value corresponds to 100 %. White areas are not measured or simulated. The 90 % of the diameter of the exit port of the integrating sphere (IS) is delimited by the white circle. Plots in the Fig. 7b) and d) are one dimensional distributions of normalized spatial intensity values (60 % - 100 %) along X-axis (red curve) and Y-axis (blue curve) cross-sections of the exit port. The 90 % of the diameter of the exit port of the IS is delimited by the green vertical lines.

In contrast to the graphical (qualitative) expression of the results comparison, the quantitative difference between the measurement and the simulation is listed in Tab. 3. For the calculation of $\mathrm{MAE}^{spatial}$ only 90 % of the exit port diameter is taken into account. This is the standard procedure in uniformity evaluation of ISs since the values near the edge of the emitting area are negatively influenced by the exit port border [33–36].

Area of the exit port	90 % **of diameter**
$\mathbf{MAE}^{spatial}$ **[%]**	0.798

Table 3: Normalized $\mathrm{MAE}^{spatial}$ (spatial radiance uniformity results of general purpose IS) values calculated according to the Eq. (7). The error values of optical simulation show the quantitative difference between results of the laboratory measurement [22] and the optical simulation, see Fig. 7. The results are presented for 90 % of the diameter of the exit port.

In Fig. 8a), 8b) and 8c) the results of the laboratory angular radiance uniformity measurement [22]

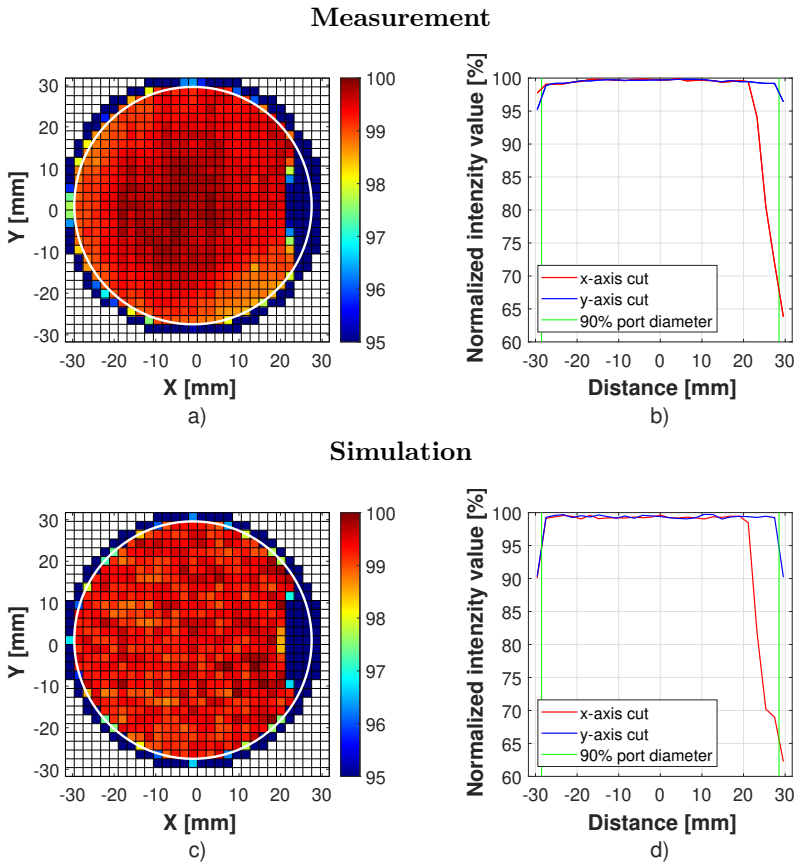

Figure 7: Comparison of the spatial radiance uniformity measurement [22] and simulation. Top color-map a) and plot b) represent the measurement and the bottom color-map c) and plot d) are the results of the simulation. Color-maps of normalized spatial intensity values are presented in fine range of 95 % - 100 % and the highest (maximum) value corresponds to 100 %. White areas are not measured or simulated. The 90 % of the diameter of the exit port of the integrating sphere (IS) is delimited by the white circle. These plots are one dimensional distributions of normalized spatial intensity values (60 % - 100 %) along X-axis (red curve) and Y-axis (blue curve) cross-sections of the exit port. The 90 % of the diameter of the exit port of the IS is delimited by green vertical lines.

are shown. In Fig. 8d), 8e) and 8f) the corresponding results acquired by the simulation are presented. Unlike the spatial radiance, the angular radiance measurement and simulation are performed following the prescription of radiance function $L(c_x, c_y, \phi, 0)$, where c_x and c_y are constant values of spatial coordinates that are used in a single measurement or simulation. Since there are fine non-symmetrical modulations of the normalized intensity values in the results, no smoothing function is used in order not to neglect any effect of the irregular geometry of general purpose IS. All plots in the Fig. 8 show the one dimensional distribution of normalized angular intensity values (65 % - 105 %) for the angular range from $-23°$ to $23°$. Values above 100 % are caused by the normalization. Unlike the normalization procedure of spatial radiance uniformity plots, the angular radiance uniformity normalization procedure is related to the value of the central spot of the exit port of IS at $0°$. This value is considered 100 % and other values are recalculated accordingly. There are two plots for each rotation position of the IS – Fig. 8a) and d) vertical, Fig. 8b) and e) diagonal and Fig. 8c) and f) horizontal which corresponds to Fig. 6. The legend of five selected representative spots of the exit port of the IS is labelled in color and number and it also corresponds to Fig. 6.

Similar to the spatial radiance uniformity results, the angular radiance uniformity results of the measurement and simulation are shown and compared numerically as well in Tab. 4. For every angular measurement (and simulation) in the selected spot of the exit port of IS (labeled as 1–5 according to the Fig. 6), there is one MAE error value. Moreover, this is performed for all three orientations of IS exit port (vertical

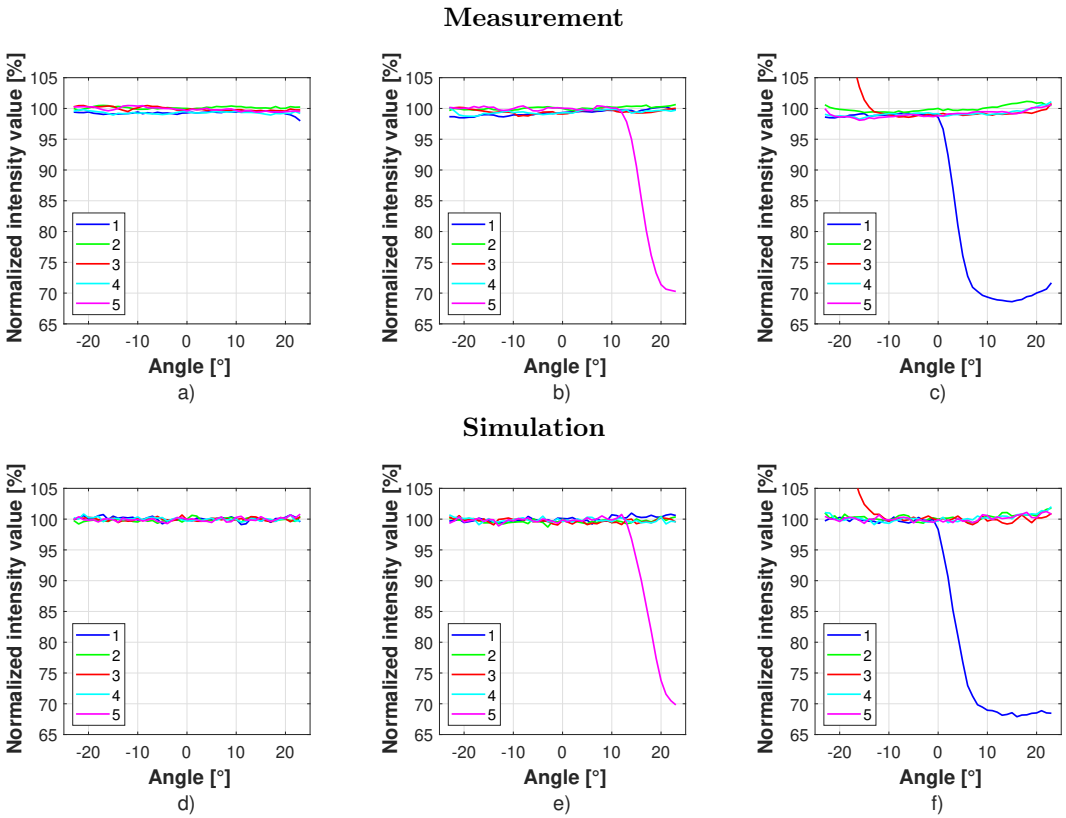

Figure 8: Comparison of angular radiance uniformity measurement [22] and simulation. Top plots represent the measurement and the bottom plots show the results of the simulation. The presented plots are one dimensional distributions of normalized angular intensity values (65 % - 105 %) with the angular range from −23° to 23° for three rotation positions of the integrating sphere (IS) – a), d) vertical, b), e) diagonal and c), f) horizontal. Each color and number of the five representative spots from the legend correspond to Fig. 6.

$\mathrm{MAE}^{vertical}$, diagonal $\mathrm{MAE}^{diagonal}$, and horizontal $\mathrm{MAE}^{horizontal}$).

Exit port position		**1**	**2**	**3**	**4**	**5**
$\mathbf{MAE}^{vertical}$	**[%]**	0.813	0.332	0.295	0.709	0.451
$\mathbf{MAE}^{diagonal}$	**[%]**	0.718	0.437	0.369	0.477	1.073
$\mathbf{MAE}^{horizontal}$	**[%]**	1.086	0.458	1.568	0.982	1.006

Table 4: Normalized $\mathrm{MAE}^{vertical}$, $\mathrm{MAE}^{diagonal}$, and $\mathrm{MAE}^{horizontal}$ (angular radiance uniformity results of general purpose IS) values calculated according to the Eq. (7). The error values of the optical simulation show the quantitative difference between results of the measurement [22] and the optical simulation, see Fig. 8. The results are presented for five selected spots in the the exit port.

4. Discussion

The beginning of the presented paper focuses on the verification of the applicability of selected optical ray-tracing software for optical simulations to the theory-based models of extended uniform light sources (EULSs). The advantage of these theory-based models, Lambertian disc (LD) and ideal integrating sphere (IS) is in their rotational symmetry. The verification is based on the cosine-fourth-power law. It describes

the decrease of the irradiance intensity at the detector plane from the center of the detector to its edge. All the results of normalized irradiance E_r/E_0 for specific testing setups match each other nearly perfectly as it is shown in Figs. 3, and 4. The agreement is numerically expressed by the normalized values of Mean Absolute Error (MAE). The normalized error values of MAE^{LD} for LD, listed in Table 1, are lower than 0.340 %. Similarly, the normalized error values of MAE^{IS} for ideal IS are listed in Table 2. The values do not exceed 0.500 %. This verifies the accuracy of the developed optical simulation models of the both LD and ideal IS and allows to proceed to more complex model of EULS.

The main part of the presented paper is devoted to the study of a real general purpose IS by Labsphere (3P-GPS-053-SL). The reason behind this choice is simple. For non-symmetrical EULSs, it is nearly impossible to compute the irradiance at a detector plane because of a complicated function of the radiance $L(x, y, \phi, \psi)$. However, in the case of this specific IS, the radiance emission profile is already well described, and thus the evaluation method of the optical simulation is adapted to match the sampling used in the laboratory radiance uniformity measurements [22]. Instead of the irradiance uniformity measurement and simulation at detector plane, the results presented in Fig. 7 and 8 are in the form of the spatial and angular radiance uniformity. In order to achieve it, the effect of two aperture radiance detector RD is simulated.

The selected optical software works with the Monte Carlo ray-tracing method based on randomly generated directions of optical rays and therefore the results are based on statistics. Thus, discrepancies between the results of laboratory measurement and optical simulation are expected due to possible fluctuation. Figure 7 shows the comparison of results of laboratory measurement and optical simulation in terms of the spatial radiance uniformity. The results of the simulation match the results of the measurement within 0.800 % according to the listed value of $\mathrm{MAE}^{spatial}$ in Tab. 3, which validates the developed optical simulation model. The only difference is the type of the spatial radiance uniformity in the color-maps. In this case, the measurement exhibits the damped type of spatial radiance uniformity (the slight decrease of normalized intensity values towards the edges), while the Monte Carlo ray-tracing simulation output is the random type of spatial radiance uniformity [34]. Since the ideal Lambertian surface (idealized model of the inner cavity of the IS) is used in the simulation, there is no reason that the result should be damped and will always be random. Therefore, this result is expected. Of course, the value of simulated uniformity depends mainly on the statistics and thus on the number of used rays. Nevertheless, the effect of the baffle is clearly observed both in the laboratory measurement and in the optical simulation. The method of simulating radiance uniformity predicts (in this case validates) what the measured radiance uniformity would be like, and thus is able to locate the sources and the level of non-uniformity.

Next to the spatial radiance uniformity results, there are the results of angular radiance uniformity, shown in Fig. 8. The precision of the model is expressed by the $\mathrm{MAE}^{vertical}$, $\mathrm{MAE}^{diagonal}$, $\mathrm{MAE}^{horizontal}$ and listed in Tab. 4. The largest error values are reaching 1.600 % and 1.100 % in spots number 3 and 1 in horizontal orientation of IS and in spot number 5 in diagonal orientation of IS. This is generally due to lower statistics, i.e., number of measured / simulated angular positions (47 positions with 1° step) and rather higher variations in angular radiance uniformity (the baffle effect and the hot spot effect). Nevertheless, this outcome is expected and overall the resulting error values are in most cases lower than 1.000 %. The plots depicting all rotation positions of IS precisely mimic all the trends (constant progress as well as increase and decrease in normalized intensity values) caused by the imperfections in rotation symmetry of the inner cavity of the general purpose IS. Similar to the spatial radiance uniformity comparison, the effect of the baffle is clearly observed also for the angular radiance uniformity measurement and simulation. The vertical rotation position in Fig. 8a) and 8d), the curves are almost constant. The diagonal rotation position in Fig. 8b) and 8e), the detector directly measures the effect of the baffle resulting in the approximate 30 % decrease in the normalized intensity values (decrease in radiance uniformity). Finally, the horizontal rotation position in Fig. 8c) and 8f), the radiance detector (RD) directly observes both the baffle and the hot spot of the primary light source on the inner surface of the IS. In case of the baffle, there is again the 30 % decrease in the normalized intensity values, thus lowering the resulting radiance uniformity by the same amount in this region. On the other hand, the hot spot leads to the rapid increase in the intensity due to the rays that are reflected directly to the detector after the first strike (only one reflection in the inner cavity of IS) compared to the rest of the surface where the integration of the light flux occurred (multiple reflections of the scattered rays). This increase in normalized intensity values is directly connected to the decrease in the

radiance uniformity since the values are off the desired range (around 100 % in an ideal case). In all three rotation positions, the developed method accurately validates the results of the laboratory measurement and is capable of locating sources of non-uniformity.

5. Conclusion

In this paper, the feasibility of extended uniform light source (EULS) simulations using OpticStudio software is verified on the examples of a Lambertian disk (LD) and an ideal integrating sphere (IS). It is based on the cosine-fourth-power law, which describes the decrease of irradiance at detector plane. The verification on both LD and ideal IS allowed to develop the simulation method that provides the information about radiance uniformity instead of the more commonly used irradiance uniformity. The major advantage of this approach is the ability to not only localize the sources of radiance non-uniformity, but also to determine their relative intensity. The accuracy of developed simulation method is validated on a real general purpose IS (3P-GPS-053-SL) by comparing the results of the optical simulation with previously measured data in optical laboratory. This comparison is based on the fact that the developed simulation model of the real IS is consistent with the measurement setup.

The ability to reliably simulate both spatial and angular radiance uniformity plays an important role in further analyses. Knowing it is plausible, the presented simulation method can be used in the virtual prototyping (optimization of possible modifications) of the EULSs in general. Furthermore, the validated simulation model of general purpose IS can be implemented into more sophisticated simulations for specialized applications using EULS. Therefore, further research on topics of virtual prototyping of EULSs is planned in the future.

Acknowledgements

The Czech authors gratefully acknowledge the support of the Ministry of Education, Youth and Sports of the Czech Republic projects LTT 18004 and CZ.02.1.01/0.0/0.0/17_049/0008422 and also Palacký University project IGA_PrF_2023_005. Further, the Czech authors gratefully acknowledge the support of the Czech Academy of Sciences and Japan Society for the Promotion of Science within the bilateral joint research project with Kyoto University (Mobility Plus project JSPS 21-10). The German authors gratefully acknowledge the support of the Bundesministerium für Bildung und Forschung (BMBF) with its funding program „Erforschung von Universum und Materie“ (ErUM) under the project number 05A20VK1.

References

[1] A. Ahmad, C. Feng, R. Sarepaka, Virtual prototyping - a cost effective emerging methodology, in: Proc. SPIE 2537, Novel Optical Systems Design and Optimization Conference, San Diego, CA, USA, Ed. Sasian, J.M., Vol. 2537, 1995, pp. 298–307.

[2] G. Wang, Definition and review of virtual prototyping, J. Comput. Inf. Sci. Eng. 2 (3) (2002) 232–236.

[3] TheScottPartnership, Optical simulation software, Nat. Photonics 4 (2010) 256–257.

[4] H. Gross, Handbook of Optical Systems, Volume 1: Fundamentals of Technical Optics, WILEY-VCH Verlag, Weinheim, 2005.

[5] F. Loosen, Design and simulation of unconventional optical systems based on ray and wave optical methods, Ph.D. thesis, Friedrich-Alexander-Universität Erlangen-Nürnberg, Erlangen, Germany (2019).

[6] Synopsys, Inc., CODE V, Mountain View, CA, 2022.
URL `https://www.synopsys.com/optical-solutions/codev.html`

[7] Zemax LLC, OpticStudio, Kirkland, WA, 2022.
URL `https://www.zemax.com/pages/opticstudio`

[8] Lambda Research Corporation, OSLO, Littleton, MA, 2022.
URL `https://lambdares.com/oslo`

[9] Lambda Research Corporation, TracePro, Littleton, MA, 2022.
URL `https://lambdares.com/tracepro`

[10] Breault Research Organization, ASAP, Tuscon, AZ, 2022.
URL `https://breault.com/asap/`

[11] Synopsys, Inc., LightTools, Mountain View, CA, 2022.
URL `https://www.synopsys.com/optical-solutions/lighttools.html`

[12] Synopsys, Inc., LucidShape, Mountain View, CA, 2022.
URL https://www.synopsys.com/optical-solutions/lucidshape.html
[13] K. Carr, Integrating sphere theory and applications - Part II.: Integrating sphere applications., JOCCA-Surf. Coat. Int. 80 (10) (1997) 485–491.
[14] Integrating sphere radiometry and photometry, Technical guide, Labsphere, North Sutton, USA (2017).
[15] Integrating sphere theory and applications, Technical guide, Labsphere, North Sutton, USA (2017).
[16] A. Ferrero, J. Campos, A. Pons, Radiance source for ccd low-uncertainty absolute radiometric calibration, in: Proceedings of the 9th International Conference of New Development and Application in Optical Radiometry, Davos, Switzerland, Gröbner, J., ed., 2005, pp. 113–114.
[17] J. Brack, R. Meyhandan, G. Hofman, J. Matthews, Absolute photometric calibration of large aperture optical systems., Astropart Phys. 20 (6) (2004) 653–659.
[18] B. Liu, Y. Yuan, Z.-Y. Yu, X. Huang, H.-P. Tan, Numerical investigation of measurement error of the integrating sphere based on the monte-carlo method, Infrared Phys. Technol. 79 (2016) 121–127.
[19] P. Foote, Illumination from a radiating disk., Bulletin of the Bureau of Standards, NBS 12 (4) (1916) 583–586.
[20] V. Mahajan, Optical Imaging and Aberrations: Part I. Ray Geometrical Optics, SPIE Press, Newburyport, 1998.
[21] K. Carr, Integrating sphere theory and applications - Part I.: Integrating sphere theory and design., JOCCA-Surf. Coat. Int. 80 (8) (1997) 380–385.
[22] M. Vacula, P. Horvath, L. Chytka, K. Daumiller, R. Engel, M. Hrabovsky, D. Mandat, H.-J. Mathes, S. Michal, M. Palatka, M. Pech, C. M. Schäfer, P. Schovanek, Use of a general purpose integrating sphere as a low intensity near-uv extended uniform light source, Optik 242 (167169) (2021) 18. doi:10.1016/j.ijleo.2021.167169.
[23] W. McCluney, Introduction to Radiometry and Photometry, Artech House, Boston, 1994.
[24] Standard for Characterization of Image Sensors and Cameras, EMVA Standard 1288-3.0, European Machine Vision Association (Nov. 2010).
[25] Getting Started With OpticStudio 15, Software guide, Zemax, LLC, Kirkland, USA (May 2015).
[26] A. Arecchi, T. Messadi, R. Koshel, Field Guide to Illumination, Volume FG11: Field Guide Series, SPIE Press, Bellingham, 2007.
[27] C. Willmott, K. Matsuura, Advantages of the Mean Absolute Error (MAE) over the Root Mean Square Error (RMSE) in Assessing Average Model Performance, Climate Research 30 (2005) 79. doi:10.3354/cr030079.
[28] LuminousOptics, FAQs - Integrating Spheres (2020).
URL http://host.web-print-design.com/sphere/german/faqs.htm
[29] General Purpose Integrating Spheres, Product guide, Labsphere, North Sutton, USA (2015).
[30] PTFE Integrating Spheres, Data sheet, Instrument Systems, Munich, Germany.
[31] Diffuse reflectance coatings and materials, Product guide, Labsphere, North Sutton, USA.
[32] Optical Society of America, Handbook of Optics, 5 Volume Set, McGraw Hill, 2009.
[33] Y. He, P. Li, G. Feng, Y. Wang, Z. Liu, C. Zheng, H. Wu, D. Sha, Computer modeling of a large-area integrating sphere uniform radiation source for calibration of satellite remote sensors., Optik 122 (13) (2011) 1143–1145.
[34] J. Jablonski, D. Scharpf, S. Rabade, L. Dobrowski, C. Durell, J. Holt, Perfectly understood non-uniformity: Methods of measurement and uncertainty of uniform sources, in: Proc. SPIE 10980, Dhar, N.K., Dutta, A.K., Babu, S.R., Eds. Conference on Image Sensing Technologies - Materials, Devices, Systems, and Applications VI, Baltimore, MD, USA, Vol. 10980, 2019, article Number: 109800I. doi:10.1117/12.2519038.
[35] Uniformity Calculations for Uniform Sources, Technical guide, Labsphere, North Sutton, USA (2019).
[36] Z. Zhang, Z. Wan, X. Li, H. Liu, J. Sun, Z. Liu, Y. Wang, J. Ren, J. Ren, Design and Characteristic Measurement of 8000 mm Large Aperture Integrating Sphere., J. Opt. Soc. Korea. 20 (4) (2016) 500–509.